Biosensor architecture for enhanced disease diagnostics: lab-in-a-photonic-crystal

Shuai Feng,[1,2] **Jian-Hua Jiang,**[1,3,*] **Abdullah Al Rashid,**[1] **and Sajeev John**[1,3,4]

[1] *Department of Physics, University of Toronto, Toronto, Ontario, M5S 1A7 Canada*
[2] *School of Science, Minzu University of China, Beijing, 100081, China*
[3] *School of Physical Science and Technology, Soochow University, 1 Shizi Street, Suzhou 215006, China*
[4] *john@physics.utoronto.ca*
[*] *joejhjiang@sina.com*

Abstract: A conceptual lab-in-a-photonic-crystal biosensor is demonstrated that can multiplex *four or more* distinct disease-markers and distinguish their presence and combinations simultaneously with unique spectral fingerprints. This biosensor consists of a photonic-band-gap, *multi-mode* waveguide coupled to surface modes on either side, encased in a glass slide with microfluidic channels. The spectral fingerprints consist of multiple peaks in optical transmission vs. frequency that respond sensitively and uniquely in both frequency shift and *nonmonotonic* change of peak transmittance levels to various analyte bindings. This special property enables complete, logical determination of *twelve* different combinations of *four* distinct disease-markers through one scan of the transmission spectrum. The results reveal unique phenomena such as switching between the strong-coupling and weak-coupling combinations of surface states by analyte binding at different locations along the central waveguide. The unconventional transmission spectra are explained using a Landauer-Büttiker, multiple-scattering, transmission theory that reproduces the main features of the exact finite-difference-time-domain simulation.

OCIS codes: (230.5298) Photonic crystals; (280.1415) Biological sensing and sensors; (170.4580) Optical diagnostics for medicine.

References and links

1. V. Pavlov, Y. Xiao, B. Shlyahovsky, and I. Willner, "Aptamer-functionalized Au nanoparticles for the amplified optical detection of thrombin," J. Am. Chem. Soc. **126**(38), 11768–11769 (2004).
2. N. A. Mortensen, S. Xiao, and J. Pedersen, "Liquid-infiltrated photonic crystals: enhanced light-matter interactions for lab-on-a-chip applications," Microfluid. Nanofluid. **4**(1), 117–127 (2008).
3. J. Vörös, J. J. Ramsden, G. Csucs, I. Szendrö, S. M. De Paul, M. Textor, and N. D. Spencer, "Optical grating coupler biosensors," Biomaterials **23**(17), 3699–3710 (2002).
4. Y. Fang, A. M. Ferrie, N. H. Fontaine, J. Mauro, and J. Balakrishnan, "Resonant waveguide grating biosensor for living cell sensing," Biophys. J. **91**(5), 1925–1940 (2006).
5. G. Peng, U. Tisch, O. Adams, M. Hakim, N. Shehada, Y. Y. Broza, S. Billan, R. Abdah-Bortnyak, A. Kuten, and H. Haick, "Diagnosing lung cancer in exhaled breath using gold nanoparticles," Nature Nanotech. **4**(10), 669–673 (2009).
6. R.-M. Ma, S. Ota, Y. Li, S. yang, and X. Zhang, "Explosives detection in a lasing plasmon nanocavity," Nat. Nanotechnol. **9**(8), 600–604 (2014).

#257100 Received 13 Jan 2016; revised 17 Feb 2016; accepted 15 May 2016; published 26 May 2016

7. J. N. Anker, W. P. Hall, O. Lyandres, N. C. Shah, J. Zhao, and R. P. Van Duyne, “Biosensing with plasmonic nanosensors,” Nat. Mater. **7**(6), 442–453 (2008).
8. J. Homola, S. S. Yee, and G. Gauglitz, “Surface plasmon resonance sensors: review,” Sens. Actuators B **54**(1), 3–15 (1999).
9. A. H. J. Yang, S. D. Moore, B. S. Schmidt, M. Klug, M. Lipson, and D. Erickson, “Optical manipulation of nanoparticles and biomolecules in sub-wavelength slot waveguides,” Nature **457**(7225), 71–75 (2009).
10. M. G. Scullion, T. F. Krauss, and A. Di Falco, “Slotted photonic crystal sensors,” Sensors **13**(3), 3675–3710 (2013).
11. N. Skivesen, A. Tetu, M. Kristensen, J. Kjems, L. H. Frandsen, and P. I. Borel, “Photonic-crystal waveguide biosensor,” Opt. Express **15**(6), 3169–3176 (2007).
12. M. Lee and P. M. Fauchet, “Two-dimensional silicon photonic crystal based biosensing platform for protein detection,” Opt. Express **15**(8), 4530–4535 (2007).
13. M. L. Adams, M. Loncar, A. Scherer, and Y. Qiu, “Microfluidic integration of porous photonic crystal nanolasers for chemical sensing,” IEEE J. Sel. Areas Commun. **23**(7), 1348–1354 (2005).
14. I. D. Block, L. L. Chan, and B. T. Cunningham, “Photonic crystal optical biosensor incorporating structured low-index porous dielectric,” Sens. and Actuators B **120**(1), 187–193 (2006).
15. M. Huang, A. A. Yanik, T.-Y. Chang, and H. Altug, “Sub-wavelength nanofluidics in photonic crystal sensors,” Opt. Express **17**(26), 24224–24233 (2009).
16. E. Yablonovitch, “Inhibited spontaneous emission in solid- state physics and electronics,” Phys. Rev. Lett. **58**, 2059–2062 (1987).
17. S. John, “Electromagnetic absorption in a disordered medium near a photon mobility edge,” Phys. Rev. Lett. **53**, 2169–2172 (1984).
18. S. John, “Strong localization of photons in certain disordered dielectric superlattices,” Phys. Rev. Lett. **58**, 2486–2489 (1987).
19. J. D. Joannopoulos, S. G. Johnson, J. N. Winn, and R. D. Meade, *Photonic Crystals: Molding the Flow of Light* (Princeton University, 2011).
20. R. D. Meade, K. D. Brommer, A. M. Rappe, and J. D. Joannopoulos, “Electromagnetic Bloch waves at the surface of a photonic crystal,” Phys. Rev. B **44**(19), 10961–10964 (1991).
21. V. N. Konopsky and E. V. Alieva, “Photonic crystal surface waves for optical biosensors,” Anal. Chem. **79**(12), 4729–4735 (2007).
22. S. Noda, M. Fujita, and T. Asano, “Spontaneous-emission control by photonic crystals and nanocavities,” Nat. Photonics **1**, 449-458 (2007).
23. M. E. Beheiry, V. Liu, S. Fan, and O. Levi, “Sensitivity enhancement in photonic crystal slab biosensors,” Opt. Express **18**(22), 22702–22714 (2010).
24. J. H. Jiang and S. John, “Photonic crystal architecture for room-temperature equilibrium Bose-Einstein condensation of exciton polaritons,” Phys. Rev. X **4**(3), 031025 (2014).
25. J. H. Jiang and S. John, “Equilibrium high-temperature Bose-Einstein condensation in dichalcogenide monolayers,” Sci. Rep. **4**, 7432 (2014).
26. M. Liss, B. Petersen, H. Wolf, and E. Prohaska, “An aptamer-based quartz crystal protein biosensor,” Anal. Chem. **74**(17), 4488–4495 (2002).
27. B. T. Cunningham, P. Li, S. Schulz, B. Lin, C. Baird, J. Gerstenmaier, C. Genick, F. Wang, E. Fine, and L. Laing, “Label-free assays on the BIND system,” J. Biomol. Screening **9**(6), 481–490 (2004).
28. M. Wilchek, E. A. Bayer, and O. Livnah, “Essentials of biorecognition: the (strept) avidinbiotin system as a model for proteinprotein and proteinligand interaction,” Immun. Lett. **103**(1), 27–32 (2006).
29. Y. Fang, “Label-free cell-based assays with optical biosensors in drug discovery,” Assay Drug Dev. Technol. **4**(5), 583–595 (2006).
30. E. Chow, A. Grot, L. W. Mirkarimi, M. Sigalas, and G. Girolami, “Ultracompact biochemical sensor built with two-dimensional photonic crystal microcavity,” Opt. Lett. **29**(10), 1093–1095 (2004).
31. A. Al Rashid and S. John, “Optical biosensing of multiple disease markers in a photonic-band-gap lab-on-a-chip: a conceptual paradigm,” Phys. Rev. Appl. **3**(3), 034001 (2015).
32. Y. Imry and R. Landauer, “Conductance viewed as transmission,” Rev. Mod. Phys. **71**(2), S306 (1999).
33. M. Büttiker, “Four-terminal phase-coherent conductance,” Phys. Rev. Lett. **57**(14), 1761–1764 (1986).
34. S. Datta, *Electronic Transport in Mesoscopic Systems* (Cambridge University, 1995).
35. C. Caroli, R. Combescot, P. Nozieres, and D. Saint-James, “Direct calculation of the tunneling current,” J. Phys. C: Solid St. Phys. **4**(8), 916–929 (1971).
36. Y. Xu, H.-B. Sun, J.-Y. Ye, S. Matsuo, and H. Misawa, “Fabrication and direct transmission measurement of high-aspect-ratio two-dimensional silicon-based photonic crystal chips,” J. Opt. Soc. Am. B **18**(8), 1084–1091 (2001).
37. Y.-J. Hung, S.-L. Lee, and L. A. Coldren, “Deep and tapered silicon photonic crystals for achieving anti-reflection and enhanced absorption,” Opt. Express. **18**(7), 6841–6852 (2010).
38. T.-M. Shih, A. Kurs, M. Dahlem, G. Petrich, M. Soljačić, E. Ippen, L. Kolodziejski, K. Hall, and M. Kesler, “Supercollimation in photonic crystals composed of silicon rods,” Appl. Phys. Lett. **93**(13), 131111 (2008).

#257100 Received 13 Jan 2016; revised 17 Feb 2016; accepted 15 May 2016; published 26 May 2016

39. L. Jiang, W. Jia, G. Zheng, and X. Li, "Design and fabrication of rod-type two-dimensional photonic crystal slabs with large high-order bandgaps in near-infrared wavelengths," Opt. Lett. **37**(9), 1424–1426 (2012).
40. S. Fan, W. Suh, and J. D. Joannopoulos, "Temporal coupled-mode theory for the Fano resonance in optical resonators," J. Opt. Soc. Am. A **20**(3), 569–572 (2003).
41. W. Suh, Z. Wang, and S. Fan, "Temporal coupled-mode theory and the presence of non-orthogonal modes in lossless multimode cavities," IEEE J. Quantum Electron. **40**(10), 1511–1518 (2004).
42. M. E. Young, P. A. Carroad, R. L. Bell, "Estimation of diffusion coefficients of proteins," Biotechnol. Bioeng. **22**(5), 947–955 (1980).
43. W.-C. Lai, S. Chakravarty, Y. Zou, and R. T. Chen, "Silicon nano-membrane based photonic crystal microcavities for high sensitivity bio-sensing," Opt. Lett. **37**(7), 1208–1210 (2012).
44. S. Chakravarty, A. Hosseini, X. Xu, L. Zhu, Y. Zou, and R. T. Chen, "Analysis of ultra-high sensitivity configuration in chip-integrated photonic crystal microcavity bio-sensors," Appl. Phys. Lett. **104**, 191109 (2014).

---

1. Introduction

Lab-on-a-chip (LoC) optical biosensors are promising paradigms for portable, convenient, and inexpensive medical testing technologies. They enable finding fatal diseases at early stages at home without requiring expensive and time-consuming laboratory medical examinations [1, 2]. Facilitated by the statistical correlation between the density anomaly of certain bio-materials (disease markers) and diseases, these biosensors can provide diagnostic tools that are non-invasive and require only a very small specimens (e.g., blood) [3–10]. The functional principle of conventional LoC optical biosensors is to detect tiny amounts of targeted biomaterials around localized optical modes through resonant frequency shifts, detected by light transmission measurements. The concentrated optical fields of localized optical modes greatly enhance light-matter interaction. The modification of local refractive index induced by tiny amounts of disease markers then leads to visible change in the transmission spectrum. Using a small scale (sub-centimeter) optical chip and scarce amounts of specimen, the LoC optical biosensor can detect the density of disease-markers and provide medical diagnosis [9–15]. The quality factor of the resonance controls the limit-of-detection of the biosensor. The strength of light-matter interaction determines the sensitivity to small amount of bio-materials.

Biosensors ideally exploit localized modes with high quality-factors that do *not* share frequencies with other spurious modes. These requirements are uniquely fulfilled for point-defect, waveguide/line-defect, and surface modes in the photonic-band-gap (PBG) of a photonic crystal [16–22]. Photonic crystals provide a versatile means of tailoring the properties of localized/guided electromagnetic modes to achieve strong light-matter interaction and a high quality-factor simultaneously [19, 22–25]. A remarkable property of PBG waveguides is that they can confine light in the low-refractive-index region (e.g., water in our biosensor). This is especially beneficial for biosensing since the analytes usually reside in the low-refractive-index region. This facilitates simultaneous realization of high sensitivity and low limit of detection, a pair of conflicting figures of merit for conventional optical sensors [1, 9].

While a full PBG is realized only for certain three-dimensional photonic crystals, two-dimensional (2D) photonic crystals can still offer a directional stop gap (2D PBG) and associated waveguide modes [18, 19]. With proper geometry for directional light injection and detection, the 2D PBG can filter out spurious modes that muddle the transmission spectra. Advanced schemes of bio-recognition such as antibody-antigen binding and DNA aptamer-protein binding have been realized recently [26–29]. If antibodies or DNA aptamers are attached to specific internal surfaces of the photonic crystal where the photonic modes are localized, accumulation of small amounts of antigen or protein will considerably modify the transmission spectrum [9].

Biosensors based on a single point-defect [12, 30] mode have demonstrated the working principles of transmission spectrum modification. However, the sensing surface area is very small in those designs, creating disadvantages such as higher limit of detection, lower sensitivity (in

#257100 Received 13 Jan 2016; revised 17 Feb 2016; accepted 15 May 2016; published 26 May 2016

terms of sample density), and long detection times (for "mouse" to find the "mouse-trap"). A possible solution is to use *(extended) guided modes* in PBG materials such as *guided surface modes* and *PBG wave-guide modes*. Surface modes often have strong light concentration and high quality-factors which provide high sensitivity. However, weakly coupled surface modes on opposite surfaces of a thick photonic crystal slab often have very low transmittance. Recently, a mechanism was demonstrated [31] to enhance the transmittance by coupling opposite surface modes using a central waveguide mode in the middle of the photonic crystal. It was shown that transmission of surface modes is highly sensitive to their coupling with the waveguide mode. This enables a novel mechanism for multi-parametric biosensing: through surface-waveguide coupling, analyte-induced frequency shift of a *single* mode also modifies hybridization with other modes, leading to *transmission enhancement/suppression of that mode*. The resulting spectral fingerprints were able to logically discriminate six different disease-marker configurations with three distinct types of analytes.

In the present paper, we demonstrate enhanced logical discrimination of twelve disease-marker configurations enabling more detailed medical diagnosis in a single measurement. Our generalized design exhibits two highly visible surface modes in the transmission spectrum, providing greater contrast between configurations. The two surface modes, the "strong-coupling" antisymmetric combination and the "weak-coupling" symmetric combination, have distinctive linewidths and frequencies. When analyte binds on only one of the chip surfaces, the strong-coupling mode has a large frequency red-shift and mild decrease of transmittance, while the weak-coupling mode has little frequency shift but distinctive transmittance change. The transmittance of the latter first decreases rapidly and then increases with further analyte binding. This characteristic is a distinguishing feature of our multiplexed biosensor.

The underlying biosensing mechanism is understood via a simplified Landauer-Büttiker mode-coupling model [32–35], which reproduces the main features of our rigorous finite-difference-time-domain (FDTD) simulation. It reveals the formation of a "strong-coupling" surface mode that concentrates hybridization with the central waveguide mode and a "weak-coupling" surface mode that minimizes this hybridization, even when the left-right mirror symmetry is broken due to unequal amounts of analyte bound to the left and right surfaces. A distinctive spectral fingerprint is that the peak transmittance level of the weak-coupling surface mode is first suppressed and then recovered with increasing binding asymmetry. Our generalized lab-in-a-photonic-crystal chip consists of *two* central waveguide modes with enriched transmission characteristics. This leads to enhanced multiplexing that can logically distinguish twelve different analyte binding configurations with four different types of disease markers.

2. Design of PBG surface and waveguide modes

The key performance metrics of a LoC biosensor are (i) the sensitivity S_m and (ii) the limit-of-detection $t_m^{(lim)}$ (associated with the m-th transmission peak) of the spectral fingerprint. The sensitivity is defined by the ratio of the frequency shift $\delta\omega_m$ to a tiny change of the analyte binding thickness τ:

$$S_m \equiv \frac{\delta\omega_m}{\tau} \equiv \omega_m \mathscr{F}_m. \tag{1}$$

Here, $\mathscr{F}_m$ (with units of inverse length), measures the optical field intensity at the analyte binding-interface. The limit-of-detection characterizes the minimum thickness of the analyte that induces a visible change in the transmission peak. It can be defined as:

$$t_m^{(lim)} \equiv \frac{\eta}{\mathscr{F}_m Q_m}, \tag{2}$$

where $\eta \sim 1$ is a dimensionless constant and Q_m is the quality-factor of the m-th mode.

#257100 Received 13 Jan 2016; revised 17 Feb 2016; accepted 15 May 2016; published 26 May 2016

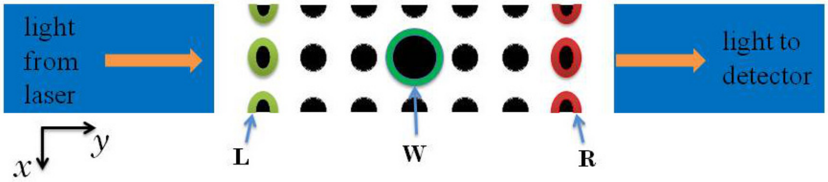

Fig. 1. Illustration of photonic crystal biosensor. The blue regions at the left and right sides are glasses. The surface layers are elliptical shaped to support surface modes. The distance between the center of the surface micro-pillars and the glass is a. The waveguide mode is introduced by a larger micro-pillar with radius $0.445a$ where a is the center-to-center distance between adjacent micro-pillars. The radius of normal micro-pillars is $0.25a$. Adjacent elliptic micro-pillars at the surface have the same semi-minor axis $0.15a$, while their semi-major axes are $0.25a$ and $0.28a$, respectively. Three different types of disease markers α, β, and σ are attached to three different analyte binding sites (labeled as "L", "R", and "W" in the figure) at the left surface, the right surface, and the central waveguide layer, separately. The length of the photonic crystal in the y direction can be $l = 3$ (as shown in the figure) or $l = 4$ (not shown).

Our photonic crystal architecture is illustrated in Fig. 1. The arrows in Fig. 1 indicate the direction of light injection and transmission. The light source and detector (spectrometer) are placed at the left and right side of the photonic crystal, respectively. The top view of the square lattice photonic crystal in one unit cell is shown in Fig. 1 where the black regions are silicon micro-pillars which are immersed in water (the white regions). The structure is periodically repeated in the x direction but finite in the y direction. There are $l = 3$ unit cells of the photonic crystal to the left and right sides of the central waveguide layer, forming a length in the y direction $L_y = (2l+1)a$ where a is the lattice constant. This type of structure has been fabricated with fine control of the pillar shape [36–39]. Water (in the region between the left and right glass slides) allows analytes (disease markers) to flow and bind to the designated pillar surfaces along the left, central and right columns. These three types of binding sites are labeled as "L", "W", and "R", respectively. The "W" sites selectively binds the σ disease marker, while the "L" ("R") binding site only binds the α (β) disease marker. Analyte-binding configurations involving more than one site are hence denoted as "LR", "LW", "RW" and "LRW". Light propagates along the y direction through the surface and waveguide modes. We assume plane waves of light with normal incidence and the detector collects all transmitted light. Analyte attachments to the three binding sites are simulated in FDTD calculation as uniform layers with thickness from 0 to $0.2a$ around the micro-pillars at the surface and central waveguide columns [see Fig. 1]. The refractive index of the analyte layers is 1.45, while the refractive index of silicon is 3.4. We take the refractive index of water and glass as 1.35 and 1.5, respectively.

The micro-pillar shapes are designed to introduce two surface modes and a waveguide mode with almost degenerate frequencies. The normal circular pillars that form the photonic crystal backbone have radii $0.25a$, while the central waveguide has alternating large pillars of radii $0.445a$. The resulting periodicity along the x direction is $2a$. Adjacent elliptic micro-pillars in the left and right columns have the same semi-minor axis $0.15a$, while their semi-major axes alternate between $0.25a$ and $0.28a$. The "period doubling" [31] in the x-direction brings the guided surface modes below the light line from the X point ($q_x = \frac{\pi}{a}$) to the Γ point ($q_x = 0$) as shown in Fig. 2(a).

The bulk photonic bands and the dispersion of each guided mode are shown in Figs. 2(a) and 2(b) [we consider only the TM mode with polarization along z direction throughout this work]. Clearly, the two surface modes and the central waveguide mode are nearly degenerate

#257100 Received 13 Jan 2016; revised 17 Feb 2016; accepted 15 May 2016; published 26 May 2016

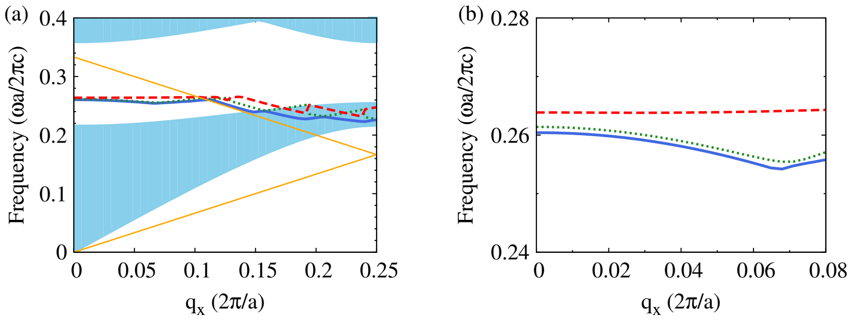

(c) waveguide mode

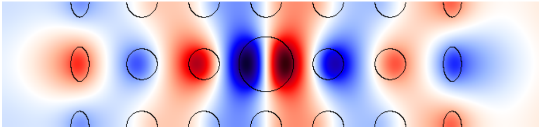

(d) antisymmetric surface mode

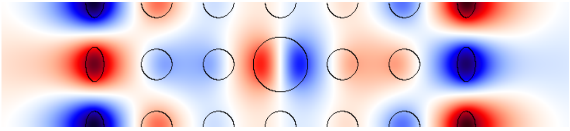

(e) symmetric surface mode

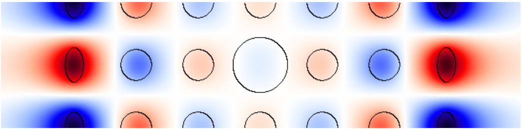

Fig. 2. (a) Band structure of the photonic crystal sensor. The blue shaded regions denote the bulk photonic bands. The red (dashed), green (dotted) and blue (solid) curves in the PBG stand for the waveguide and (two) surface guided modes, separately. The yellow solid line denotes the light line in glass. Period doubling in the x direction folds the region $\frac{\pi}{2a} < q_x \leq \frac{\pi}{a}$ back to the first Brillouin zone $-\frac{\pi}{2a} < q_x \leq \frac{\pi}{2a}$. As a consequence the surface and waveguide modes originally below the light line are moved to above the light line which are then able to couple to light in glass. Since the structure possess left-right mirror symmetry, the two surface modes form the anti-symmetric (blue curve) and symmetric (green curve) modes, respectively. The field distribution of the waveguide and surface modes are illustrated in (c)-(e). The frequencies of the anti-symmetric surface mode, the symmetric surface mode and the waveguide mode at $q_x = 0$ are 0.2605, 0.2613 and 0.2640 (in unit of $\frac{2\pi c}{a}$) separately. The length of the photonic crystal in the y direction is $l = 3$.

#257100 Received 13 Jan 2016; revised 17 Feb 2016; accepted 15 May 2016; published 26 May 2016

near $q_x = 0$. For the chosen parameters, there is a frequency range, 0.22 to 0.36 (in units of $\frac{2\pi c}{a}$) (finite-size effect reduces this window to 0.25 to 0.28) where the transmission is negligible for nearly normal incidence ($q_x \sim 0$). This 2D PBG filters out other modes and (in the absence of disorder) the transmission comes exclusively from the two surface modes and the waveguide mode. The electric field E_z distributions of those modes are plotted in Figs. 2(c)–2(e). The waveguide mode is anti-symmetric in the y direction. The two surface modes can be expressed as anti-symmetric and symmetric linear combinations. Due to the anti-symmetric nature of the waveguide mode, it couples primarily with the anti-symmetric surface mode, but not with the symmetric surface mode (opposite to the situations considered by Rashid and John in [31] where the waveguide mode is symmetric in the y-direction). The field distributions plotted in Figs. 2(c)–2(e) are those of the hybridized modes. Clearly, the anti-symmetric surface mode has considerable field strength near the central waveguide, whereas the symmetric surface mode is much weaker near the central waveguide.

The qualitative features of the field distribution can be understood from a simple mode hybridization theory. The "photon Hamiltonian" can be written as

$$\hat{H} = \begin{pmatrix} \omega_\ell & t_{\ell r} & t_{\ell w} \\ t_{\ell r} & \omega_r & t_{rw} \\ t_{\ell w} & t_{rw} & \omega_w \end{pmatrix}, \tag{3}$$

where ω_i ($i = \ell, r, w$) are the resonance frequencies of the left surface-mode, the right surface-mode, and the central waveguide mode at the wave-vector $q_x = 0$, $t_{\ell r}$ is the direct tunnel coupling between the two surface modes, $t_{\ell w}$ (t_{rw}) is the tunnel coupling between the left (right) surface mode and the waveguide mode. These off-diagonal elements are determined by the overlap integrals of the field distributions for different modes. Because the waveguide mode is anti-symmetric along the y direction, the coupling coefficients, $t_{\ell w}$ and t_{rw}, have *opposite* sign. It is more illustrative to describe the system with symmetric $|S\rangle$ and anti-symmetric $|AS\rangle$ surface states, which gives

$$\hat{H}' = \begin{pmatrix} \omega_{AS} & 0 & \sqrt{2}t_{\ell w} \\ 0 & \omega_S & 0 \\ \sqrt{2}t_{\ell w} & 0 & \omega_w \end{pmatrix}, \tag{4}$$

where $\omega_{AS} = \omega_\ell - t_{\ell r}$ and $\omega_S = \omega_\ell + t_{\ell r}$. In the absence of asymmetric analyte binding all the interaction between surface modes and the waveguide mode is "concentrated" in the anti-symmetric surface mode, while the symmetric surface mode does *not* couple to the waveguide mode. The eigen-frequencies of the model system are:

$$\Omega_w = \omega_w + \sqrt{2}|t_{\ell w}|, \quad \Omega_{AS} = \omega_\ell - t_{\ell r} - \sqrt{2}|t_{\ell w}|, \quad \Omega_S = \omega_\ell + t_{\ell r}, \tag{5}$$

where Ω_w is the frequency of the waveguide-like mode, Ω_{AS} and Ω_S denote the frequencies of the anti-symmetric and symmetric surface-like modes, respectively.

3. Single-mode waveguide sensor transmission spectrum

In this section we demonstrate some striking features of transmission spectra in response to analyte bindings in our photonic crystal biosensor using a $l = 3$ chip with a single waveguide mode. The unique spectral fingerprint due to surface-waveguide mode-coupling provides distinctive determination of various combinations of disease markers.

We first study the response of transmission spectrum to analyte binding at the central waveguide, the W-binding. Figure 3(a) reveals three resonance peaks, resulting from hybridization of the surface and central waveguide modes. Their field distributions reveal that the rightmost peak

#257100 Received 13 Jan 2016; revised 17 Feb 2016; accepted 15 May 2016; published 26 May 2016

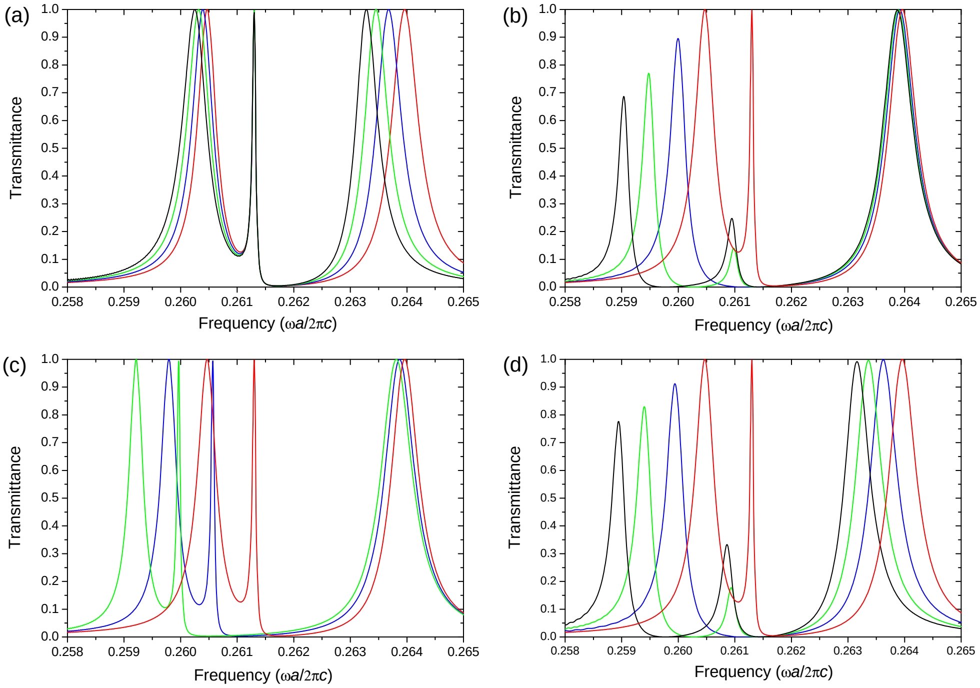

Fig. 3. Transmission responses to analyte binding for different binding configurations. The right-most peak is dominated by the central waveguide mode, whereas the central peak arises from the weak-coupling surface mode, and the left-most peak is dominated by the strong-coupling surface mode. (a) When analyte σ is bound to the W site at the central waveguide. (b) When analyte α is bound to the L site at the left surface of the photonic crystal. (c) When analytes α and β bind to the L and R sites at the surfaces with equal thickness. (d) When analytes α and σ bind to both the L and W sites. From red, blue, green to black, the thickness of analyte layer is 0, $0.05a$, $0.1a$, and $0.15a$, respectively. For (a) and (c), the system has mirror symmetry and the strong-coupling (weak-coupling) surface mode is the anti-symmetric (symmetric) combination of the left and right surface modes. In comparison, for (b) and (d), the mirror symmetry is broken, the strong-coupling (weak-coupling) surface mode is no longer the anti-symmetric (symmetric combination of the left and right surface modes, but other mixture of the two. The length of the photonic crystal along the y direction is $l = 3$.

#257100 Received 13 Jan 2016; revised 17 Feb 2016; accepted 15 May 2016; published 26 May 2016

is the waveguide-like mode, the leftmost peak corresponds to the anti-symmetric surface-like mode, while the central peak stands for the symmetric surface mode. The symmetric surface mode has a much higher quality-factor than the other two modes. For $l = 3$, the quality-factor of the central waveguide mode is too low for practical applications, but useful to demonstrate the underlying physics of the observed spectral features. In Sec. V we study the $l = 4$ chip with two central waveguide modes where the quality-factors are much higher and more favorable for practical applications.

The anti-symmetric surface mode in the $l = 3$ chip has a low quality-factor due to its strong hybridization with the low quality-factor waveguide mode. When the disease marker σ is attached to the W binding site, the resonance peak of the waveguide-like mode shifts toward lower frequencies. This also induces a red-shift of the anti-symmetric surface-like mode, while the symmetric surface mode does *not* respond to the analyte binding at the W site. The interaction between the waveguide mode and the anti-symmetric surface mode "pushes" the latter toward lower frequency. Analogous behaviour was reported in an alternative design [31] where, instead, the symmetric surface mode hybridizes strongly with the central waveguide mode.

Due to the left-right mirror symmetry, our biosensor does not distinguish between disease marker α binding at the left surface L sites (see Fig. 3(b)) and the disease marker β binding at the right surface R sites. The induced spectral features are unique to our biosensor design and distinct from conventional sensors as well as the multi-parametric biosensor studied earlier [31]. The leftmost peak shifts continuously to lower frequencies as the thickness of the disease marker α is increased. In contrast, the frequency of the central peak only moves slightly. The transmittance level of the leftmost peak continuously decreases, whereas the transmittance level of the central peak *first decreases and then increases*. In Fig. 3(b) this manifests as *disappearance and reappearance* of the central peak with analyte layer thickness. This non-monotonic variation and nontrivial modification of transmission of one channel (the central peak) due to frequency-shift of another channel (the leftmost peak) is a *distinguishing feature* of our photonic crystal biosensor. It differs from the monotonic changes of transmission with analyte-binding shown in [31] and is explained using a Landauer-Büttiker mode-coupling theory [32–35] in Sec. 4. The key role of surface-waveguide coupling in those spectral fingerprints is demonstrated in Appendix: A.

The transmission response of equal amounts of disease markers α and β to both L and R sites (same thickness of analytes) is shown in Fig. 3(c). The two surface-like modes (the left peak and the central peak) shift to lower frequency together. The peak transmittance levels of the two modes do not reduce because the mirror symmetry in the y direction is kept.

When disease markers α and σ attach to both the left surface (L site) and the waveguide (W site), we observe [see Fig. 3(d)] both red-shift of the waveguide mode and distinctive disappearance and reappearance of the central peak, due to the weak-coupling surface mode.

The responses in the transmission spectrum (peak-frequency shifts and transmission level variations) to different disease marker combinations are summarized in Table 1. Our single-waveguide-mode photonic crystal biosensor can logically discriminate between six disease marker combinations within a single transmission measurement through the chip. The detailed spectral fingerprints are easily discernible due to high quality-factor resonances. The nonmonotonic variation of transmission through the weak-coupling surface mode (central peak) is also more apparent in the circular-post design. This spectral signature corresponds to the splitting of the surface-mode resonance in the square-post design [31], but is now much easier to resolve. At the same time, there is reduction of transmission level and (significant) red-shift of the strong-coupling (leftmost) peak. The reduction of transmission levels of the two surface modes is characteristic of *asymmetric* analyte binding. In contrast, if disease markers α and β bind symmetrically on the L and R sites, the peak transmittance of the two surface modes

#257100 Received 13 Jan 2016; revised 17 Feb 2016; accepted 15 May 2016; published 26 May 2016

Table 1. Diagnostic logic table using three disease markers in the $l = 3$ biosensor with a single central waveguide mode. Changes in peak frequencies and transmittance in response to various analyte-binding configurations are tabulated. The frequency shift of the waveguide mode, Ω_w, (right peak), the strong-coupling surface mode, Ω_{sc}, (left peak), and the weak-coupling surface mode, Ω_{wc}, (central peak), together with changes in peak transmission levels, T_{sc} and T_{wc}, of the latter two surface modes, provide distinct spectral fingerprints of different analyte-binding configurations. The symbol ↓:↑ denotes that peak transmission first decreases then increases.

Analyte-binding configuration	Ω_w	Ω_{sc}	Ω_{wc}	T_{sc}	T_{wc}
no binding	|	|	|	—	—
σ binding only	←	|	|	—	—
$(\alpha \oplus \beta)$ & $(\neg\, \sigma)$	|	←	←	↓	↓:↑
$(\alpha \oplus \beta)$ & σ	←	←	←	↓	↓:↑
$(\alpha$ & $\beta)$ & $(\neg\, \sigma)$	|	←	←	—	—
α & β & σ	←	←	←	—	—

is undiminished as they red-shift. The quantitative spectral fingerprints of resonance frequency shifts and transmission level changes are summarized in Appendix B. The optimal length of the chip along the y direction is discussed in Appendix C.

4. Mode-coupling interpretation of spectral fingerprints

To understand the nonmonotonic transmission level change of the weak-coupling surface mode, we employ the Landauer-Büttiker multiple scattering theory [32–35]. We reduce the transmission through our biosensor into a simplified effective model with only three coupled modes, since the PBG effectively suppresses tunneling through the chip via other states. The Landauer-Büttiker theory is more general than the temporal coupled-mode theory [19, 40, 41] and our previous perturbative treatment of light scattering [31]. It includes all possible multiple scattering paths in contrast to single-pass tunneling involving second-order perturbation theory [31]. The nonmonotonic behavior of peak transmission level *cannot* be explained within the single-pass tunneling theory. As shown in Appendix D, the dominant tunneling trajectory changes during the nonmonotonic variation of the peak transmission level.

In the n-mode Landauer-Büttiker model, the transmission spectrum is given by the trace of a product of $n \times n$ matrices [34]

$$T(\omega) = \mathrm{Tr}(\hat{\Gamma}_L \hat{G}_r \hat{\Gamma}_R \hat{G}_a). \tag{6}$$

Here, the matrix $\hat{\Gamma}_L$ describes scattering rates from the photon continuum in the left-side glass to the n modes in the photonic crystal chip. The two photonic Green's functions $\hat{G}_r$ and $\hat{G}_a$ describe multiple scattering/tunneling between the n modes within the chip. Finally, $\hat{\Gamma}_R$ describes scattering rates from the chip into the photonic continuum in the right-side glass. The photonic Green's functions are given explicitly by:

$$\hat{G}_r = [\omega - \hat{H} + \frac{i}{2}(\hat{\Gamma}_L + \hat{\Gamma}_R)]^{-1}, \quad \hat{G}_a = \hat{G}_r^{\dagger}. \tag{7}$$

In the case of only three guided modes in the chip, the photon Hamiltonian is given by Eq. (3). The resonance frequencies in Eq. (3) ω_i ($i = \ell, r, w$) can be extracted from FDTD calculation. The photon hopping energy from the left surface mode to the right surface mode $t_{\ell r}$ is estimated

#257100 Received 13 Jan 2016; revised 17 Feb 2016; accepted 15 May 2016; published 26 May 2016

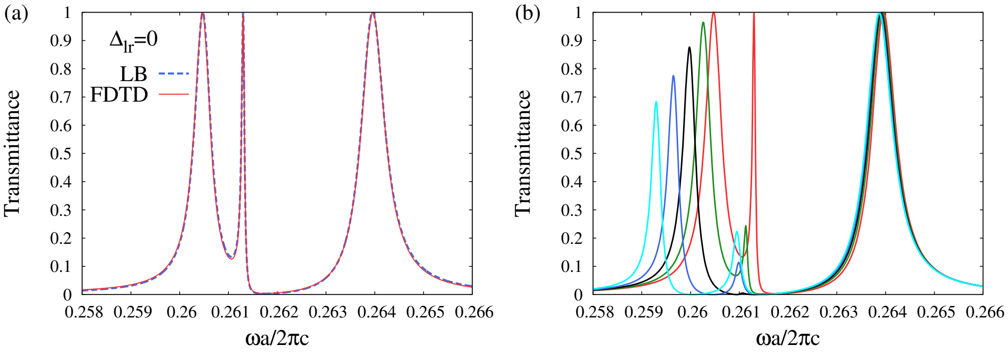

Fig. 4. Calculation of transmission using a simplified three-mode Landauer-Büttiker model in the $l = 3$ chip with a single central waveguide mode. (a) Comparison between Landauer-Büttiker theory (dashed curve) and FDTD calculation (solid curve) for no analyte binding. Parameters are given in the main text. (b) Transmission from the Landauer-Büttiker theory for different analyte binding asymmetries $\Delta_{\ell r} \equiv \omega_\ell - \omega_r$ (varying ω_ℓ with ω_r fixed). $\Delta_{\ell r} =$ 0 (red), 0.4 (green), 0.8 (black), 1.2 (blue), and 1.6 (cyan) (in unit of $10^{-3} \times (2\pi c)/a$).

from the FDTD calculation (for the structure without the central waveguide) as half of the frequency splitting of the two surface modes. We find that, without analyte binding, the parameters for the biosensor are $\omega_\ell = \omega_r = 0.26118$, $\omega_w = 0.26338$, and $t_{\ell r} = 1.3 \times 10^{-4}$ (in units of $\frac{2\pi c}{a}$). To reproduce the splitting between the strong-coupling and weak-coupling surface modes, we set $t_{\ell w} = -t_{rw} = 9.2 \times 10^{-4}(2\pi c/a)$.

The $\hat{\Gamma}_L$ ($\hat{\Gamma}_R$) matrix describes the rates at which the three modes scatter into the photonic continuum in the left (right) glass. Explicitly, they can be written as [35, 41]

$$\hat{\Gamma}_\nu = 2\pi\rho_\nu V_\nu^\dagger V_\nu, \quad \nu = L, R \tag{8}$$

where ρ_ν ($\nu = L, R$) is the density of states of the photonic continuum in the left/right glass, $V_\nu = (V_{\nu,\ell}, V_{\nu,r}, V_{\nu,w})$ describes the coupling between the photonic continuum with the localized states in the photonic crystal chip. From the mirror symmetry of the surface and waveguide modes, the relationships between the coupling coefficients can be deduced,

$$V_{L,\ell} = V_{R,r}, \quad V_{L,r} = V_{R,\ell}, \quad V_{L,w} = -V_{R,w}. \tag{9}$$

For simplicity we ignore the coupling between the left photonic continuum and the right surface state $V_{L,r}$, and similarly $V_{R,\ell}$, because tunneling through the photonic crystal is suppressed by the PBG. The FDTD transmission spectra is fitted best when $V_{L,w} : V_{L,\ell} : V_{L,r} = -2.15 : 0.84 : 0$ and $2\pi\rho_\nu(\sum_{i=w,\ell,r} |V_{\nu,i}|^2) = 5.33 \times 10^{-4}(2\pi c/a)$ for $\nu = L, R$ [see Fig. 4(a)]. The Landauer-Büttiker theory also faithfully reproduces the nonmonotonic behavior of the peak transmission level of the weak-coupling surface mode [see Fig. 4(b)] when the disease marker α binds to the L site. This binding configuration induces a red-shift of left surface mode, which is modeled in Fig. 4(b) by the frequency change $\omega_\ell \to \omega_r - \Delta_{\ell r}$ with $\Delta_{\ell r}$ standing for the frequency difference between the left and right surface modes.

5. Multi-mode waveguide sensor with enhanced multiplexing

To enhance the diagnostic capability of our biosensor, we introduce an architecture with two central waveguide modes [see Fig. 5(a)]. The electric fields E_z of the eigen-modes are plotted in Figs. 5(b) and 5(c). The two waveguide modes are introduced by using two enlarged

(a) Schematic of device

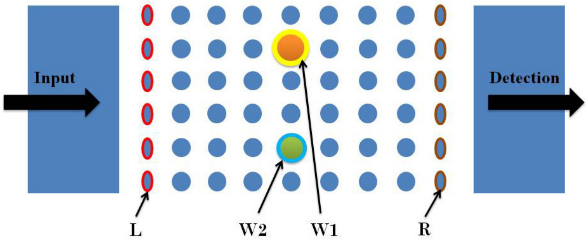

(b) waveguide modes

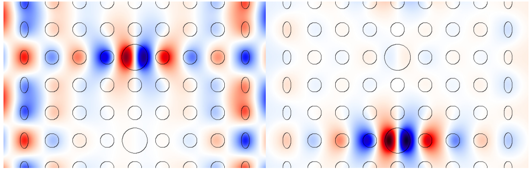

(c) surface modes

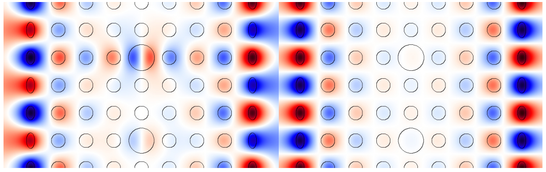

Fig. 5. (a) Illustration of photonic crystal sensor with two central waveguide modes and enlarged unit cell. Four different analyte binding sites are labeled as “L”, “W1”, “W2”, and “R”. The radii of the two enlarged micro-pillars in the middle are $r_1 = 0.47a$ (W1) and $r_2 = 0.455a$ (W2), respectively. (b) and (c): Electric field E_z distribution of the waveguide and surface modes from plane-wave-expansion calculation for the case with *no* analyte binding. At $q_x = 0$, the w_1 waveguide mode has frequency $0.2591(\frac{2\pi c}{a})$, the w_2 waveguide mode has frequency $0.2628(\frac{2\pi c}{a})$, the anti-symmetric surface mode has frequency $0.2614(\frac{2\pi c}{a})$, and the symmetric surface mode has frequency $0.2618(\frac{2\pi c}{a})$. Note that these frequencies are slightly different from the peak frequencies in the FDTD calculation. The length of the photonic crystal in the y direction is $l = 4$. The structure is periodically repeated in the x (vertical) direction.

micro-pillars separated in space with the radii $r_1 = 0.47a$ (upper) and $r_2 = 0.455a$ (lower), respectively, in each unit cell. These radii are chosen such that one waveguide mode has frequency higher than the surface modes, while the other waveguide mode has frequency lower than the surface modes. The structure exhibits mirror symmetry in the y direction, but breaks the mirror symmetry in the x direction. Direct coupling between the two surface modes is negligible for this design with $l = 4$. Nevertheless, as shown below, in many situations the surface-waveguide coupling can split the degeneracy of the two surface modes, separating them into the symmetric and anti-symmetric superposition states. The electric field distributions of the symmetric and anti-symmetric surface states have visible differences: In Fig. 5(c), the anti-symmetric surface mode has considerable fraction of field near the two modes of the central waveguide, while the symmetric surface mode has negligible field strength there. Moreover, the symmetric superposition of surface modes does not interact or hybridize with the waveguide modes due to symmetry-induced orthogonality.

We show that the strong-coupling and weak-coupling surface modes picture remains valid, even when analyte binding further breaks the mirror symmetries of the system and the surface

#257100 Received 13 Jan 2016; revised 17 Feb 2016; accepted 15 May 2016; published 26 May 2016

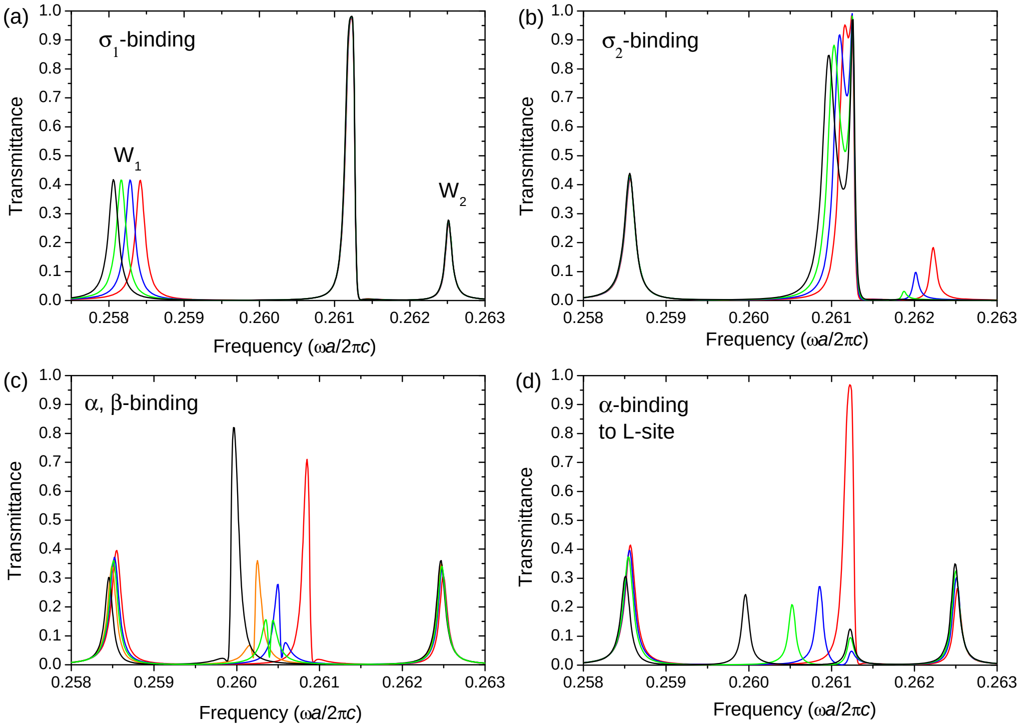

Fig. 6. Transmission spectra for different analyte binding combinations in the $l = 4$ photonic crystal biosensor with two central waveguide modes: (a) analyte σ_1 is attached to the W1 site (see Fig. 5), (b) analyte σ_2 is attached to the W2 site, (c) analyte α and β are attached to the L and R sites at the surfaces with equal thickness, (d) analyte α binds to the L site. The red, blue, green, orange, to black curves in each figure represent different thicknesses of disease markers: (a) 0.025*a*, 0.05*a*, 0.075*a*, and 0.1*a*; (b) 0.05*a*, 0.1*a*, 0.15*a*, and 0.2*a*; (c) 0.025*a*, 0.0375*a*, 0.05*a*, 0.0605*a*, 0.075*a*, and 0.1*a*; (d) 0, 0.025*a*, 0.05*a*, and 0.1*a*.

modes are no longer symmetric and anti-symmetric superpositions. The two waveguide modes, in the course of coupling with surface modes, form strong-coupling and weak-coupling superpositions as well. That is, one superposition of the waveguide modes concentrates the coupling with the surface modes, while the other superposition minimizes the coupling with the surface modes.

We first study the situation when only the disease marker σ_1 is bound to the upper waveguide mode (denoted as w_1), i.e., the W1 binding site. From Fig. 6 only the leftmost peak (i.e., the w_1 waveguide mode) is shifted, while other peaks remain unmodified. In this case the biosensor acts as a conventional resonance-shift biosensor.

For pure W1 binding the splitting between the strong-coupling and weak-coupling surface modes is barely visible due to their finite linewidth and relatively weak surface-waveguide coupling, compared to the architecture with a single central waveguide mode. As more σ_1 disease marker binds to site W1, the w_1 waveguide mode shifts to lower frequency, away from the surface modes. This effect leads to even weaker hybridization with the surface modes. In addition, the peak transmission levels of the two waveguide modes are reduced. This is mainly because, in the present case, the waveguide modes have significantly different profile (due to dielectric periodicity of 6 along x direction) compared with the surface modes (with

#257100
Received 13 Jan 2016; revised 17 Feb 2016; accepted 15 May 2016; published 26 May 2016

(a) central waveguide modes

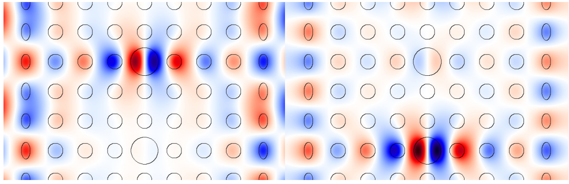

(b) surface modes

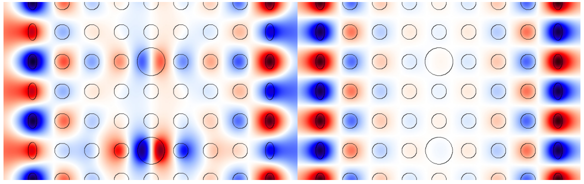

Fig. 7. Electric field E_z distributions of the (a) central waveguide modes and (b) surface modes (from plane-wave-expansion calculations) for the case with disease marker σ_2 binding to the W2 site with thickness $0.2a$. At $q_x = 0$, the upper waveguide mode (w_1) has frequency $0.2591(\frac{2\pi c}{a})$, while the lower waveguide mode (w_2) has frequency $0.2619(\frac{2\pi c}{a})$. The anti-symmetric surface mode has frequency $0.2613(\frac{2\pi c}{a})$, while the symmetric surface mode has frequency $0.2618(\frac{2\pi c}{a})$. Note that these frequencies are slightly different from the peak frequencies obtained by FDTD simulations.

dielectric periodicity of 2). When photons enter one waveguide mode from the left surface mode or leave that waveguide mode through the right surface mode, they suffer considerable filtering, rendering reduced transmission even at resonances. Our calculation indicates that reducing the width of the chip along the y direction does not improve the transmission level of the waveguide modes [see Appendix C]. The filtering effect implies that adding more central waveguide modes for a given set of surface modes will lead to even further reduction of the overall transmission signal in each channel.

For disease marker σ_2 binding to the W2 site, however, both the rightmost peak and the peaks in the middle are affected. This is because the antisymmetric (strong coupling) surface mode couples more strongly with the W2 site than the W1 site [see Fig. 7]. The frequency of the rightmost peak (corresponding to the waveguide mode w_2) is reduced and its transmission level is suppressed. As the rightmost peak approaches the central peak (corresponding to the surface modes), the splitting between the strong-coupling (anti-symmetric) and weak-coupling (symmetric) surface modes increases: the strong-coupling surface mode shifts to lower frequency whereas the weak-coupling surface mode does not move. This splitting occurs because disease marker σ_2 binding to the W2 site preserves the mirror symmetry in the y direction. Consequently, the weak-coupling symmetric surface mode remains nearly orthogonal to the waveguide modes. In contrast, the strong-coupling antisymmetric surface mode is pushed lower in frequency by the waveguide mode w_2 as this waveguide mode approaches it in frequency.

It may seem surprising that the responses are so different for analyte binding on the W1 site compared to analyte binding on the W2 site. From the field distribution in Fig. 5(c), in the case of no analyte binding, the antisymmetric surface mode exhibits stronger hybridization with the w_1 than the w_2 waveguide mode. However, a more careful examination of the field profiles of the modes for the case of analyte binding to the W2 site with thickness $0.2a$ [see Fig. 7] reveals that as analyte binds to the W2 site and the w_2 mode shifts toward the surface modes, the anti-symmetric surface mode interacts and hybridizes more strongly with the w_2 mode than with the w_1 mode. From Fig. 7(b), the anti-symmetric surface mode has much larger field distribution

Received 13 Jan 2016; revised 17 Feb 2016; accepted 15 May 2016; published 26 May 2016

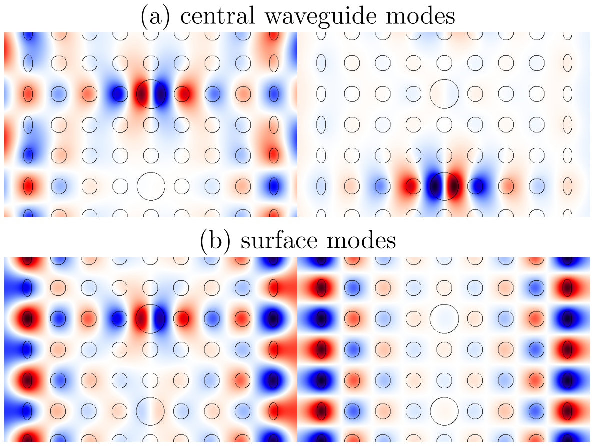

Fig. 8. Electric field E_z profiles of the (a) central waveguide modes and (b) surface modes (from plane-wave-expansion calculations) for analyte binding to the L and R sites with equal thickness $0.1a$. At $q_x = 0$, the w_1 waveguide mode has frequency $0.2590(\frac{2\pi c}{a})$, the w_2 waveguide mode has frequency $0.2628(\frac{2\pi c}{a})$, the anti-symmetric surface mode has frequency $0.2609(\frac{2\pi c}{a})$, and the symmetric surface mode has frequency $0.2601(\frac{2\pi c}{a})$. These frequencies are slightly different from the peak frequencies obtained by FDTD simulation.

at the w_2 waveguide mode than at the w_1 waveguide mode. The enhanced interaction between the w_2 mode and the anti-symmetric surface mode pushes the anti-symmetric surface mode to lower frequency and enhances the splitting between the anti-symmetric and symmetric surface modes.

We now study the situation when the disease markers α and β are bound to the L and R sites with equal thickness (so that the structure retains mirror symmetry in the y direction. In this configuration, the two surface modes (central peaks) shift simultaneously to lower frequency. This frequency shift enhances the coupling between the anti-symmetric surface mode and the w_1 waveguide mode (the leftmost peak), whereas it reduces the coupling between the anti-symmetric surface mode and the w_2 waveguide mode (the rightmost peak). This change leads to intriguing modification of transmission levels of the surface modes. With small amounts of LR-binding, the anti-symmetric surface mode is mainly repulsed by the w_2 waveguide mode, so its frequency is lower than that of the symmetric surface mode. This appears in the surface mode transmission spectra as a higher left-central peak and a lower right-central peak. The left-central anti-symmetric surface mode has higher transmission because there are additional transmission paths through hybridization with waveguide modes [see Fig. 6].

When analyte binding at the L and R sites pulls the surface modes frequencies close to the w_1 waveguide mode, the resulting strong interaction and repulsion between the anti-symmetric surface mode and the w_1 waveguide mode renders the anti-symmetric surface mode with higher frequency than the symmetric surface mode. In this situation, the transmission spectrum of the surface modes exhibits a lower left-central peak and a higher right-central peak. This understanding is confirmed by the field profiles of different modes for a large analyte thickness of $0.1a$. In Fig. 8, the anti-symmetric surface mode has much stronger hybridization with the w_1 mode. Our calculation from plane-wave-expansion also confirms that the anti-symmetric surface mode has higher frequency than the symmetric one.

We now turn to the situation when the disease marker α is bound to the L site (or equivalently, the disease marker β is bound to the R site). As the amount of analyte increases, the left and right surface modes gradually become independent. When the surface modes decouple and

#257100
Received 13 Jan 2016; revised 17 Feb 2016; accepted 15 May 2016; published 26 May 2016

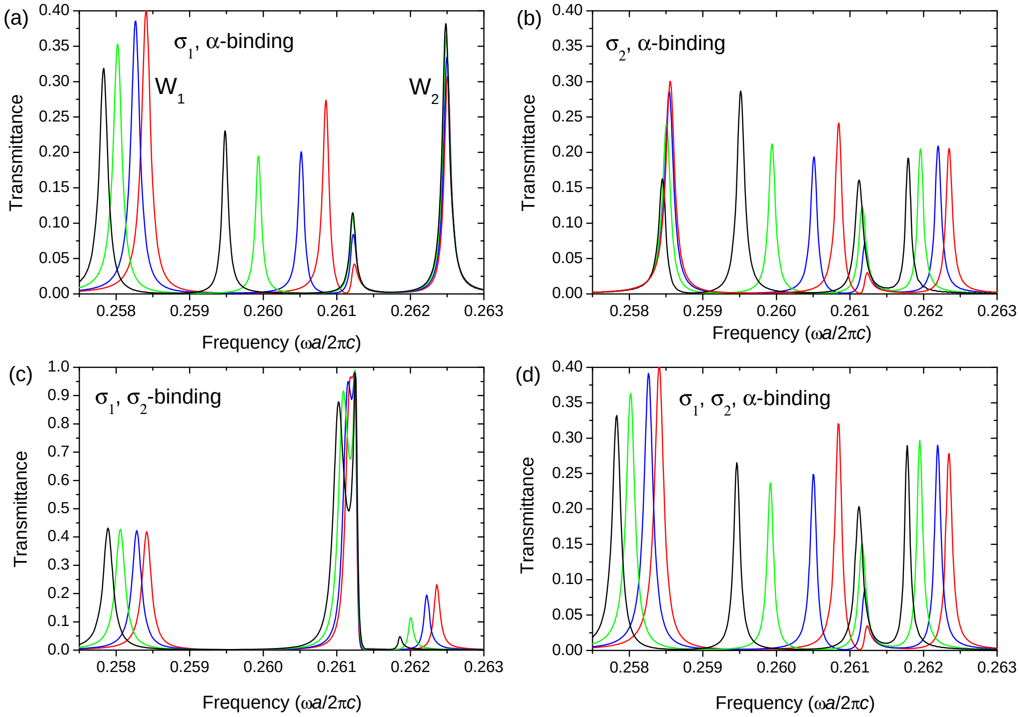

Fig. 9. Transmission responses of different two-analyte binding configurations for the $l = 4$ biosensor with two central waveguide modes: (a) analytes σ_1 and α bind to the W1 and L sites, respectively (b) analytes σ_2 and α bind to the W2 and L sites, respectively (c) analytes σ_1 and σ_2 bind to the W1 and W2 sites, respectively (d) analytes α, σ_1, and σ_2 bind to the L, W1, and W2 sites, respectively. The red, blue, green, and black curves in each figure represent different thicknesses of disease markers: (a) 0.025*a*, 0.05*a*, 0.1*a*, and 0.15*a*; (b) 0.025*a*, 0.05*a*, 0.1*a*, and 0.15*a*; (c) 0.025*a*, 0.05*a*, 0.1*a*, and 0.15*a*; (d) 0.025*a*, 0.05*a*, 0.1*a*, and 0.15*a*.

the left surface mode approaches the w_1 waveguide mode (the leftmost peak) its transmission level increases again due to enhanced coupling with the w_1 waveguide. This enhanced coupling slightly red-shifts the leftmost peak (the w_1 waveguide mode).

The transmission spectral fingerprints of other more complicated combinations of disease markers are shown in Figs. 9 and 10. In general, the features there are (almost) combinations of those in Fig. 6. To further demonstrate that the surface modes form strong-coupling and weak-coupling superpositions even when mirror symmetry in the y direction is broken, we plot in Fig. 11 the field profiles for analyte binding to the L, W1, and W2 sites with thickness 0.15*a*. Clearly, the surface mode with lower frequency (mostly left surface mode with weak admixture of the right surface mode) has much stronger hybridization with the waveguide modes. In contrast, the right surface mode (with higher frequency) has little mixing with the left surface mode and the waveguide modes. The lower frequency surface mode corresponds to the strong-coupling surface mode, while the higher frequency surface mode is the weak-coupling surface mode. Moreover, the w_1-like waveguide mode hybridizes with the surface modes much more than the w_2-like waveguide mode. Hence, the former is a strong-coupling waveguide mode, whereas the latter is a weak-coupling waveguide mode.

We summarize the spectral fingerprints of our biosensor in Table 2. From these character-

#257100 Received 13 Jan 2016; revised 17 Feb 2016; accepted 15 May 2016; published 26 May 2016

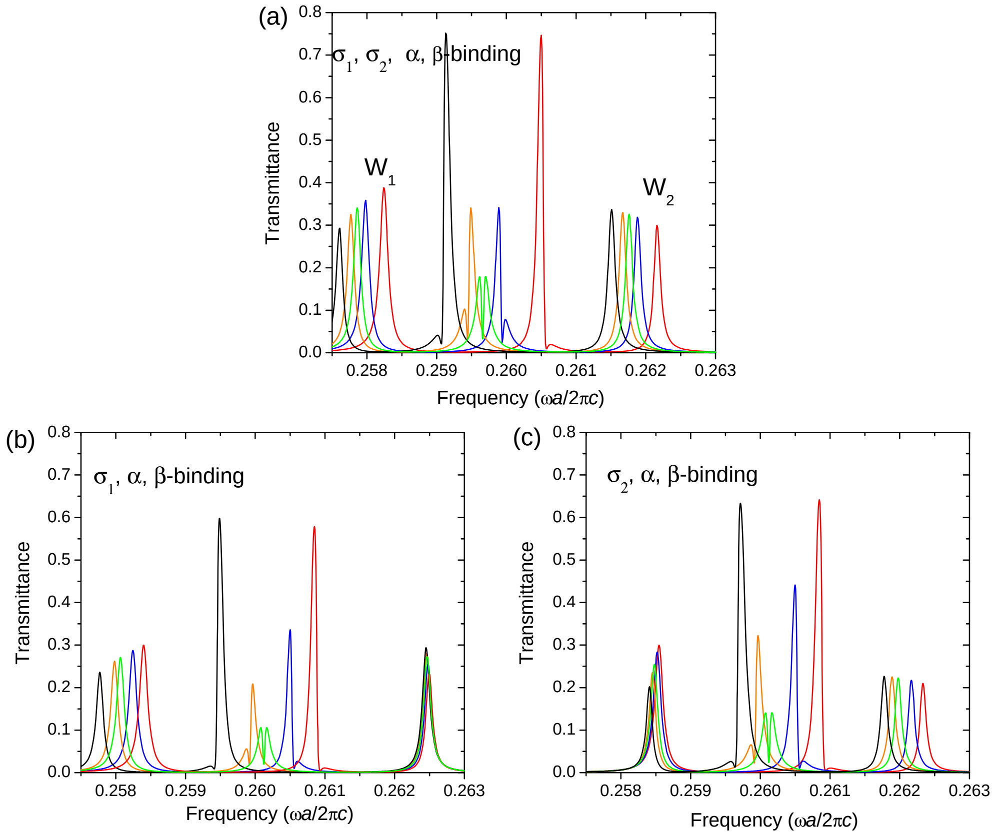

Fig. 10. Transmission spectra for different three-analyte binding combinations: (a) analytes are bound to all sites with equal thickness, (b) analytes are bound to all except the W2 site with equal thickness, (c) analytes are bound to all except the W1 site with equal thickness. From the red, blue, green, orange, and black curves in each figure represent different thicknesses of disease markers: (a) $0.05a$, $0.1a$, $0.12675a$, $0.15a$, and $0.2a$; (b) $0.025a$, $0.05a$, $0.0827a$, $0.1a$, and $0.15a$; (c) $0.025a$, $0.05a$, $0.0828a$, $0.1a$, and $0.15a$.

istics, one can logically discriminate 12 different disease marker combinations, allowing for detailed diagnosis of diseases. While enabling a higher level biomarker multiplexing than previous designs [31], the spectral fingerprints in our biosensor remain highly visible and distinctive.

We study the quantitative spectral fingerprints of resonance frequency shifts and transmission level changes for 11 different combinations of disease marker binding in Appendix B. From data in Appendix B we estimate the sensitivity (from the slope of the resonance frequency vs. disease marker thickness) of the s_1 surface mode to disease marker α to be $S_{s1} = 0.012\frac{2\pi c}{a^2}$. For $a = 1\mu$m, we find that $S_{s1} = 2.3 \times 10^{10}$ Hz nm^{-1}. The quality-factor of the surface mode is estimated from the transmission spectrum as 2100 [from Fig. 6(d)]. Therefore the limit-of-detection is $t_s^{(lim)} = 10$ nm [if $\eta = 1$ in Eq. (2)]. The longest distance for a disease marker to travel in order to reach a binding site in our biosensor is $10a$ (i.e., the width in the y direction for $l = 4$ chip). For $a \sim 1\mu$m and disease marker diffusion constant in water [42] of $\sim 10^{-10}$ m^{2}s^{-1}, it takes about 1 second to reach the binding site (after the chip is immersed in the sample liquid). For a practical photonic crystal sensor with ~ 20 supercell periods in the x direction, the total

#257100
Received 13 Jan 2016; revised 17 Feb 2016; accepted 15 May 2016; published 26 May 2016

Table 2. Logic table for enhanced medical diagnosis using four disease markers in the $l = 4$ biosensor with two central waveguide modes. Here we show how the peak frequencies and transmission levels change in response to the increase of analyte-layer thickness for the 12 analyte-binding configurations. The leftmost, middle-left, middle-right, and rightmost peaks in the transmission spectrum are denoted as w_1, s_1, s_2, and w_2. Their frequencies are denoted as Ω_{w1}, Ω_{s1}, Ω_{s2}, and Ω_{w2}, and their peak transmission levels are denoted as T_{w1}, T_{s1}, T_{s2}, and T_{w2}. We use the symbol $\downarrow$:$\uparrow$ to represent that the transmission level first decreases then increases.

Analyte-binding configuration	Ω_{w1}	Ω_{s1}	Ω_{s2}	Ω_{w2}	T_{w1}	T_{s1}	T_{s2}	T_{w2}
No binding	$\vert$	$\vert$	$\vert$	$\vert$	—	—	—	—
σ_1 binding only	$\leftarrow$	$\vert$	$\vert$	$\vert$	—	—	—	—
σ_2 binding only	$\vert$	$\leftarrow$	$\vert$	$\leftarrow$	—	$\downarrow$	—	$\downarrow$
$(\alpha \,\&\, \beta) \,\&\, (\neg\sigma_1) \,\&\, (\neg\sigma_2)$	$\vert$	$\leftarrow$	$\leftarrow$	$\vert$	$\downarrow$	$\downarrow$	$\uparrow$	$\uparrow$
$(\alpha \oplus \beta) \,\&\, (\neg\sigma_1) \,\&\, (\neg\sigma_2)$	$\vert$	$\leftarrow$	$\vert$	$\vert$	$\downarrow$	$\downarrow$:$\uparrow$	$\downarrow$:$\uparrow$	$\uparrow$
$(\alpha \oplus \beta) \,\&\, \sigma_1 \,\&\, (\neg\sigma_2)$	$\leftarrow$	$\leftarrow$	$\vert$	$\vert$	$\downarrow$	$\downarrow$:$\uparrow$	$\downarrow$:$\uparrow$	$\uparrow$
$(\alpha \oplus \beta) \,\&\, (\neg\sigma_1) \,\&\, \sigma_2$	$\vert$	$\leftarrow$	$\vert$	$\leftarrow$	$\downarrow$	$\downarrow$:$\uparrow$	$\downarrow$:$\uparrow$	$\vert$
$(\neg\alpha) \,\&\, (\neg\beta) \,\&\, \sigma_1 \,\&\, \sigma_2$	$\leftarrow$	$\leftarrow$	$\vert$	$\leftarrow$	—	$\downarrow$	—	$\downarrow$
$(\alpha \oplus \beta) \,\&\, \sigma_1 \,\&\, \sigma_2$	$\leftarrow$	$\leftarrow$	$\vert$	$\leftarrow$	$\downarrow$	$\downarrow$:$\uparrow$	$\downarrow$:$\uparrow$	—
$\alpha \,\&\, \beta \,\&\, \sigma_1 \,\&\, \sigma_2$	$\leftarrow$	$\leftarrow$	$\leftarrow$	$\leftarrow$	$\downarrow$	$\downarrow$	$\uparrow$	$\uparrow$
$\alpha \,\&\, \beta \,\&\, \sigma_1 \,\&\, (\neg\sigma_2)$	$\leftarrow$	$\leftarrow$	$\leftarrow$	$\vert$	$\downarrow$	$\downarrow$	$\uparrow$	$\uparrow$
$\alpha \,\&\, \beta \,\&\, (\neg\sigma_1) \,\&\, \sigma_2$	$\vert$	$\leftarrow$	$\leftarrow$	$\leftarrow$	$\downarrow$	$\downarrow$	$\uparrow$	$\uparrow$

width in x direction is $\sim 120\ \mu$m (if $a \simeq 1\mu$m). Since the length of each biosensor segment is on the scale of $\sim$100μm, it is in principle possible to integrate nearly 100 segments in a single biosensing chip with an overall length scale of $\sim$ 1 cm. Each biosensor segment can have different sensing functions by using different analyte bindings. A laser beam with a spot-size diameter of 100 μm can be scanned over the entire chip. The whole device can offer a logical diagnosis for complex diseases without recourse to external laboratory testing.

In realistic situations, several effects may reduce the quality of the biosensor. The first one is the fabrication imperfection which induces scattering loss and reduction of the quality factor of the waveguide and surface modes. With current photonic crystal fabrication technology, this effect can be controlled and reduced. Very high quality-factor (exceeding 10000) localized modes in photonic crystals have been achieved and exploited for biosensing in [43]. The second one comes from absorption of light by water or analytes. Absorption by water is shown to be negligible for wavelength around 1500 nm [44]. Analytes are regarded as non-absorbing in this work (because analytes absorbing light can be detected more easily using its absorption).

6. Conclusions and discussion

Using a photonic crystal lab-on-a-chip architecture we have demonstrated a conceptual paradigm for disease diagnostics using combinations of four distinct biomarkers. Using FDTD simulation, we calculate the spectral responses of our biosensor to different analyte binding configurations and quantify their spectral fingerprints. It was first shown for a biosensor with a single central waveguide mode that 6 different combinations of disease markers can be distinguished with highly visible and differentiated characteristics in the transmission spectrum. We then showed that for the design with two waveguide modes in a single unit cell, 12 different combinations of disease markers can be unambigously identified. The underlying phys-

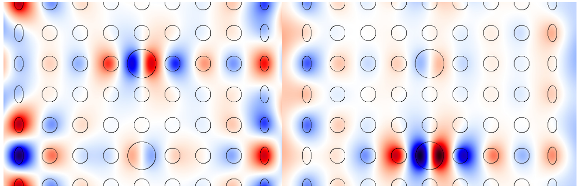

(a) central waveguide modes

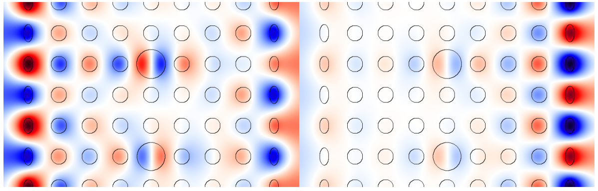

(b) surface modes

Fig. 11. Electric field E_z distributions of the (a) central waveguide modes and (b) surface modes from plane-wave-expansion calculations for the case with analytes binding to the L, W1, and W2 sites with equal thickness $0.15a$. At $q_x = 0$, the upper waveguide mode (w_1) has frequency $0.2590(\frac{2\pi c}{a})$, the lower waveguide mode (w_2) has frequency $0.2620(\frac{2\pi c}{a})$, the left surface mode has frequency $0.2603(\frac{2\pi c}{a})$, and the right surface mode has frequency $0.2616(\frac{2\pi c}{a})$. These frequencies are slightly different from the peak frequencies obtained by FDTD simulations.

ical mechanism is based on the interaction and hybridization of surface and central waveguide modes. The transmission spectra and field distributions reveal the presence of a strong-coupling linear combination of surface modes that concentrates interaction and hybridization with the central waveguide modes. On the other hand, a weak-coupling linear combination of surface modes minimizes interaction and hybridization with the central waveguide modes. The intricate modifications in hybridization and coupling between resonance modes give rise to striking, disease-specific, spectral fingerprints in our biosensor. These include frequency shift and transmission level changes of a mode, induced by the frequency shift of another mode, in response to analyte binding. These correlated spectral responses are key ingredients of our disease-marker multiplexing. The spectral fingerprints are highly distinguishable using a microfluidic chip with a complete photonic band gap.

Our conceptual 2D design demonstrates the principles of enhanced multiplexing for a lab-in-a-photonic-crystal. In any real 3D system, a mechanism for light-confinement in the vertical (z-direction) is also required. A simple glass encasing of the liquid region above and below the 2D photonic crystal (consisting of vertical pillars) will cause light to be guided around the detection region due to the higher refractive index of glass relative to water. If the pillars are very long in the z-direction, diffraction of light will occur in the vertical direction. In either case, the coupling of light to the analyte binding region will be weak. Refractive index guiding of light can be achieved in the z-direction by inserting a thin planar slab of high-index material at the $z = 0$ plane (center) of the 2D photonic crystal, with fluid regions above and below the planar slab. However, this typically leads to low quality resonances in the transmitted signal. These factors underscore the requirement for a true 3D photonic crystal with additional dielectric periodicity in the vertical direction. When such a 3D lab-in-a-photonic-crystal possesses a complete 3D PBG, strong light confinement in the vertical direction is possible and high-quality optical resonances are realized. Such an optical biosensor, utilizing a 3D PBG and highly robust to the effects of structural disorder, will be presented elsewhere.

#257100 Received 13 Jan 2016; revised 17 Feb 2016; accepted 15 May 2016; published 26 May 2016

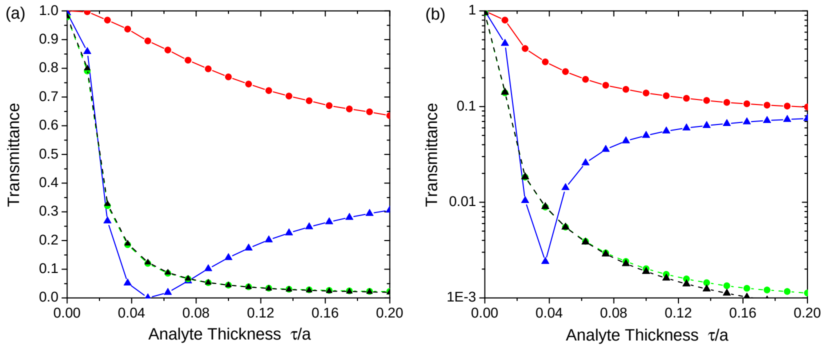

Fig. 12. Importance of surface-waveguide coupling is demonstrated via the peak transmittance at the two surface modes when the disease marker α is attached to the left surface (the L binding site) for (a) $l = 3$ and (b) $l = 4$ chip. The solid curves (red and blue) are for structures with the (single-mode) central waveguide, whereas the dashed curves (black and green) are for structures *without* the central waveguide. Curves with ● stands for peak transmittance at the lower frequency surface mode, whereas curves with △ represent peak transmittance at the higher frequency surface mode. The vertical axis of (b) is on log-scale.

A. Importance of surface-waveguide coupling

In Fig. 12 we plot the transmission levels of the two surface modes as functions of analyte layer thickness at the L binding site. To demonstrate the importance of the surface-waveguide coupling for biosensing, we also plot the transmission levels of the surface modes of a chip *without* the waveguide mode in the middle. For the latter case, the transmittance through both surface modes decay quickly when ω_ℓ and ω_r are tuned off-resonance, which is a common phenomenon in off-resonance sequential tunneling. In the presence of the waveguide mode, the transmission level of the weak-coupling surface mode first decreases rapidly. However, when the frequency difference $\Delta_{\ell r}$ further increases, the transmission level of the weak-coupling surface mode is gradually recovered. At large $\Delta_{\ell r}$ the transmission level of the weak-coupling mode is already considerable. The disappearance and recovery of the weak-coupling surface mode in the transmission spectrum adds valuable functionality to our biosensor. In contrast, for the chip *without* the central waveguide mode the transmission levels of the surface modes decrease monotonically and vanish quickly with analyte binding asymmetry.

B. Quantitative features of transmission spectral fingerprints

B.1. Single-waveguide-mode biosensor

The quantitative transmission spectral characteristics for the single-waveguide-mode biosensor are explored in Fig. 13. Figure 13(a) shows the ubiquitous resonance frequency shift for the central waveguide mode for analyte binding at the W site. The resonance frequency of the strong-coupling surface mode is red-shifted whenever there is analyte binding at the L or R surface (or both) as indicated in Fig. 13(b). In contrast, the resonance frequency of the weak-coupling surface mode can only be red-shifted when analytes are bound to both L and R surfaces [see Fig. 13(c)]. The peak transmittance level for both the strong-coupling and weak-coupling surface modes can be used as a measure of asymmetric analyte binding at the left and right surfaces. While the transmittance of the strong-coupling surface mode decreases monotonically when the asymmetry increases, the transmittance of the weak-coupling surface mode first decreases dramatically (to almost zero) and then recovers gradually. At large analyte thickness, the transmittance of the two surface modes is comparable. However, the strong-coupling

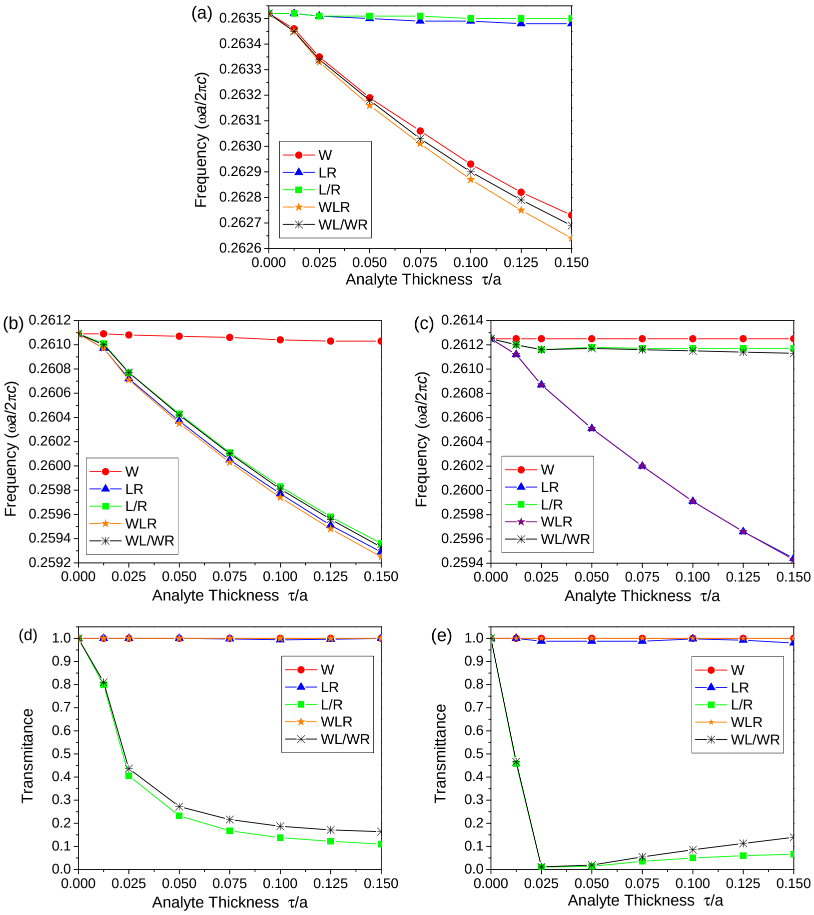

Fig. 13. Quantitative transmission spectral signatures of our biosensor with a single central waveguide and $l = 4$. (a) Resonance frequency of the central waveguide mode vs. analyte thickness for different binding configurations. (b) and (c): resonance frequencies of the strong-coupling surface mode (left peak) and the weak-coupling surface mode (central peak) as functions of analyte thickness. (d) and (e): transmission level of the strong-coupling surface mode and the weak-coupling surface mode as functions of analyte thickness.

surface mode exhibits much more red-shift than the weak-coupling surface mode.

B.2. Double-waveguide-mode biosensor

Quantitative features of transmission spectral fingerprints for the double-waveguide-mode biosensor are explored in Figs. 14 and 15. For the waveguide mode w_1, the red-shift of the resonance frequency is mostly induced by the analyte binding at the W1 site. Analyte binding at the surface sites L and R may also induce red-shift of the resonance frequency of w_1 but only slightly. Similarly, red-shift of the resonance frequency of the w_2 waveguide mode is only induced by analyte binding at the W2 site. The effect of surface analyte binding on the w_2 waveguide resonance frequency is negligible. However, analyte binding at L and R sites has strong effects on the peak transmission levels of the central waveguide modes w_1 and w_2. While analyte binding on the W1 site has negligible effect on peak transmission level of the

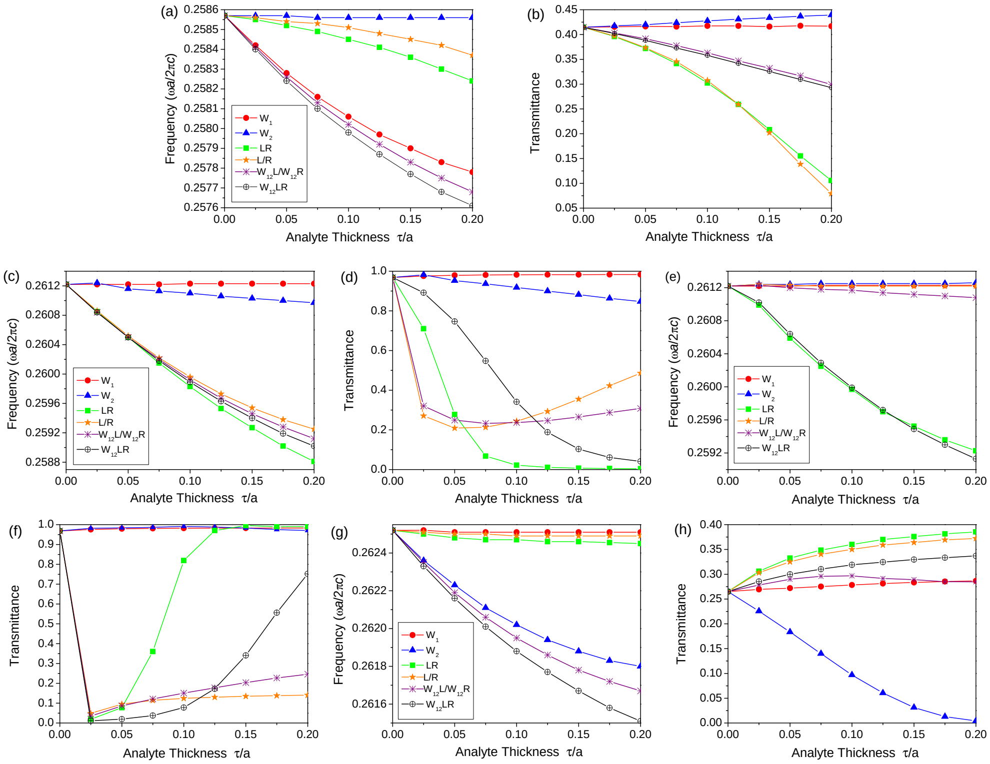

Fig. 14. Quantitative transmission spectral fingerprints of the $l = 4$ biosensor with two central waveguide modes in response to six different disease marker combinations. Resonance frequency (a) and transmission level (b) of the central waveguide mode w_1 as functions of analyte binding thickness for various analyte binding configurations. Note that "W_{12}" in the figure stands for W1+W2, i.e., analytes bind simultaneously to sites W1 and W2. Resonance frequency (c) and transmission level (d) of the surface mode s_1 (left-central peak) as functions of analyte thickness. Resonance frequency (e) and peak transmittance (f) of the surface mode s_2 (right-central peak) as functions of analyte thickness. Resonance frequency (g) and transmission level (h) of the central waveguide mode w_2 as functions of analyte thickness.

w_1 waveguide mode, analyte binding at the W2 site can suppress the transmission peak of the w_2 waveguide mode. This difference between the two central waveguide modes can be used to differentiate analyte binding at the W1 and W2 sites.

For the two-waveguide-mode case, the strong-coupling surface mode red-shifts considerably in response to asymmetric surface analyte binding, whereas red-shift of the weak-coupling surface mode is negligible. When analytes α and β attach to the L and R sites with equal thickness, both surface modes red-shift together. This symmetric binding has the opposite effect on surface mode peak transmittance: the right-central peak is suppressed while the left-central peak is enhanced. This switching between the strong-coupling and weak-coupling surface mode is explained in the main text.

One distinction of the double-waveguide-mode biosensors is that the peak transmission level of the strong-coupling surface mode is also nonmonotonic when analyte is bound asymmetrically to the L and R sites. This is caused by the enhanced coupling with the waveguide mode of w_1 when the strong-coupling surface is close to w_1 in frequency. These detailed spectral

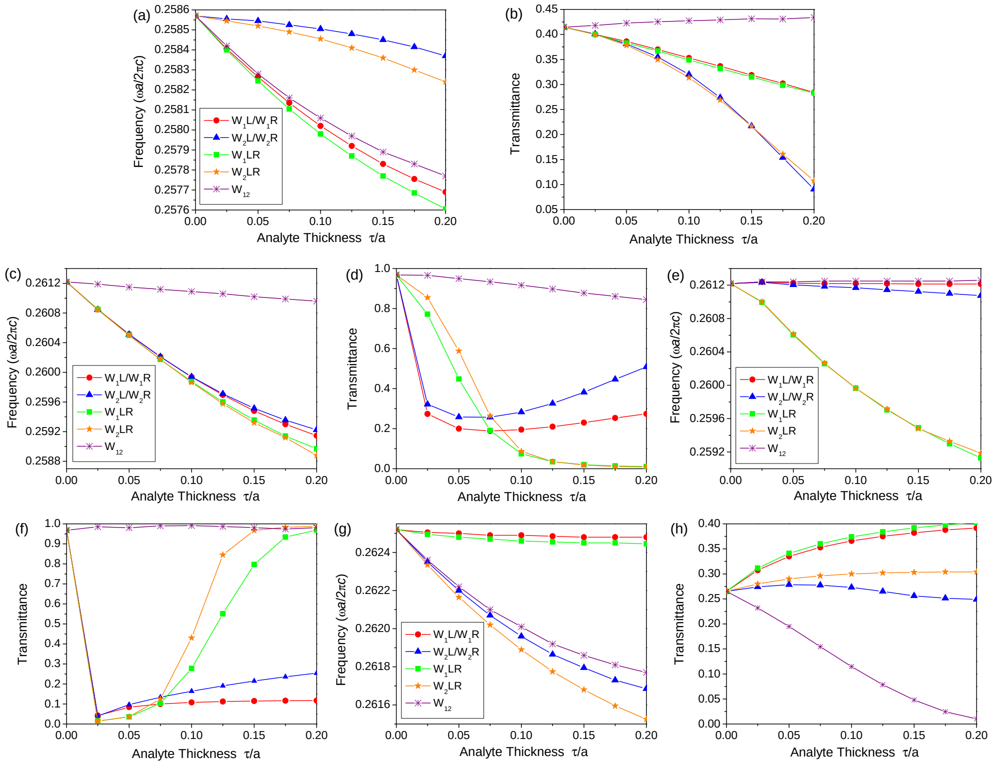

Fig. 15. Quantitative transmission spectral signatures of the $l = 4$ biosensor with two central waveguide modes in response to further disease marker combinations.

signatures greatly enrich the logic table (Table 2) for medical diagnosis.

C. Optimization of chip width

For the photonic crystal biosensor with a single waveguide mode, the $l = 4$ chip gives the best balance between quality-factor of resonances and waveguide-surface coupling. The higher quality-factor gives rise to smaller limit-of-detection according to Eq. (2). The quality-factor of resonances is improved through further increasing the width of the photonic crystal chip in the y direction. However, this reduces the coupling between the localized surface and waveguide modes, as the distance between surface and central waveguide increases.

From Fig. 16 one can see that the resonance peaks are highly visible in the transmission spectra. The effect of surface-waveguide coupling is also manifested in the splitting between the two surface modes and the nonmonotonic transmission level change when disease marker α is attached to the binding site L. The quality factor of 800 for the $l = 4$ chip is much larger than 280 of the $l = 3$ chip. This quality factor is increased to 7000 for the $l = 4$ chip with square-posts [31].

Further increase in width of the photonic crystal chip along the y direction leads to negligible waveguide-surface coupling, which degrades the multiplexing capability of the biosensor. For example, the $l = 5$ chip has only one transmission peak for the two surface modes because of much weaker surface-waveguide coupling.

The optimal width of the biosensor chip with two waveguide modes is likewise $l = 4$. Increasing the width along the y direction to $l = 5$ suppresses surface-waveguide coupling and

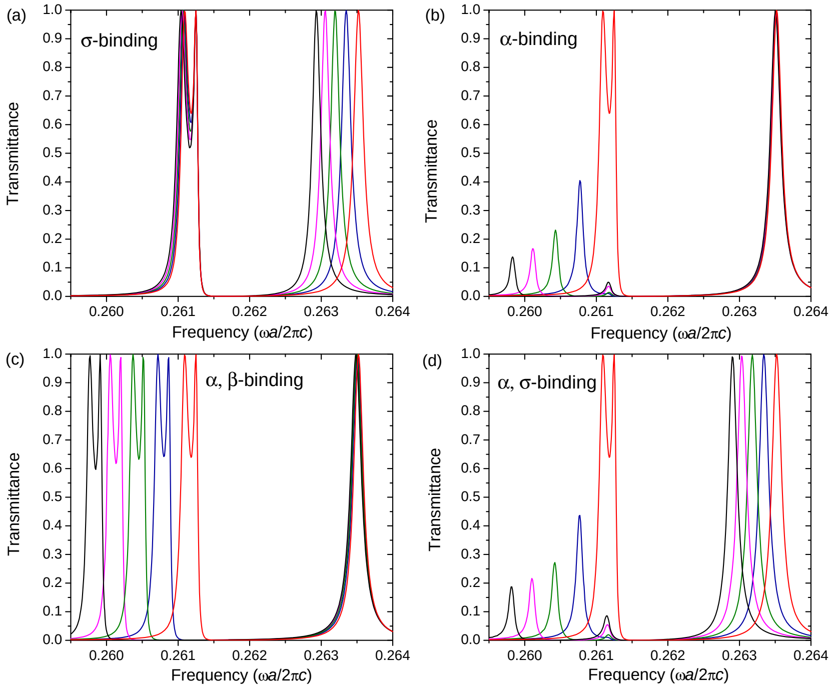

Fig. 16. Transmission spectral responses in the $l = 4$ chip with one central waveguide mode, to different disease-marker configurations: (a) disease marker σ attached to the site W, (b) disease marker α bound to the binding site L, (c) disease markers α and β attached to the binding sites L and R with equal thickness, respectively, (d) disease markers α and σ bound to the sites L and W with equal thickness, respectively. Red, blue, green, magenta, and black curves correspond to the thicknesses of the disease marker layers of 0, 0.025*a*, 0.05*a*, 0.075*a*, and 0.1*a*, respectively.

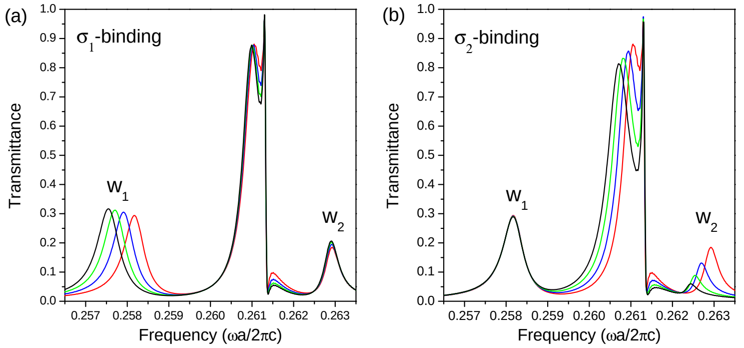

Fig. 17. Transmission spectral responses to different disease-marker configurations for photonic crystal biosensor with two central waveguide modes and (reduced) width $l = 3$ in the *y* direction: (a) analyte σ_1 attached to the W1 site, (b) analyte σ_2 attached to the W2 site. Red, blue, green, and black curves in each figure represent different thickness of disease markers: 0, 0.05*a*, 0.1*a*, and 0.15*a*.

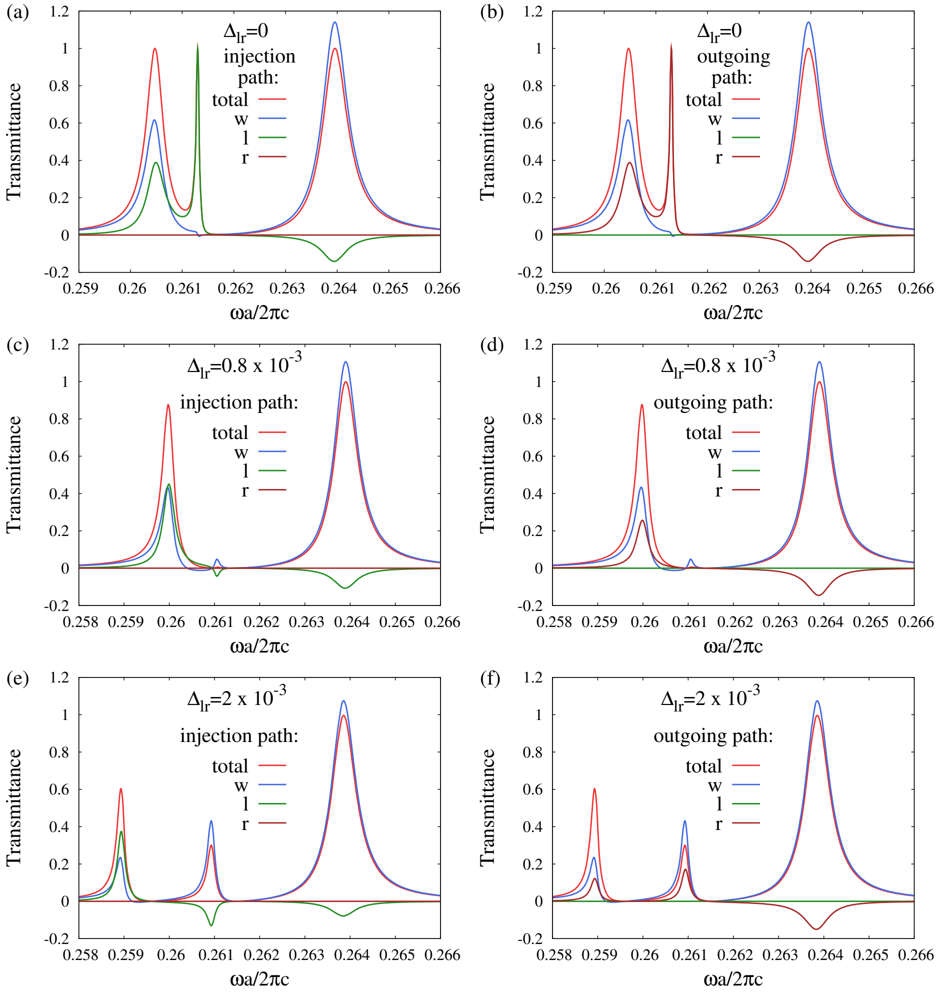

Fig. 18. Transmission spectra from Landauer-Büttiker theory for the $l = 3$ chip with single central waveguide mode, $T(\omega)$ (red) and $T_i(\omega)$ [or $\tilde{T}_i(\omega)$], $i = w, \ell, r$, for different analyte binding asymmetries $\Delta_{\ell r} = 0$ (a) and (b), $\Delta_{\ell r} = 0.8 \times 10^{-3}(2\pi a/c)$ (c) and (d), $\Delta_{\ell r} = 2 \times 10^{-3}(2\pi a/c)$ (e) and (f).

degrades the multiplexing functionality. Reducing the width along the y direction to $l = 3$, significantly reduces the quality-factor of the guided surface and waveguide modes. In addition, the $l = 3$ chip does not have improved transmission level for the central waveguide mode, as shown in Fig. 17. The lower transmission level for the two-waveguide sensor is explained (see main text) as due to wave filtering effects. It is worth mentioning that although the chip width is optimized for the frequency's of surface and waveguide modes, we did not optimize the quality factor to improve the sensitivity of the sensor. Such optimization can be achieved by shifting the frequency's of surface and waveguide modes closer and increasing the chip width. In that regime, the quality factors are higher while the coupling between modes is weaker.

#257100 Received 13 Jan 2016; revised 17 Feb 2016; accepted 15 May 2016; published 26 May 2016

D. Transmission trajectories in the Landauer-Büttiker theory

The Landauer-Büttiker theory includes all multiple scattering paths that contribute to transmission. Insertion of projection operators $\hat{P}_i = |i\rangle\langle i|$ $(i = \ell, r, d)$ into the trace at the left of $\hat{\Gamma}_L$ in Eq. (6) picks out the contribution to transmission through a specific path. When photons are injected from the left glass into the guided mode i in the chip, this partial transmission, denoted as $T_i(\omega) \equiv \mathrm{Tr}(\hat{P}_i\hat{\Gamma}_L\hat{G}_r\hat{\Gamma}_R\hat{G}_a)$, may be negative at some frequencies (reflecting destructive interference between different paths). However, the total transmission $T(\omega) = \sum_i T_i(\omega)$ is always positive. Similarly, we project on the outgoing paths by $\tilde{T}_i(\omega) \equiv \mathrm{Tr}(\hat{\Gamma}_L\hat{G}_r\hat{\Gamma}_R\hat{P}_i\hat{G}_a)$, and again $T(\omega) = \sum_i \tilde{T}_i(\omega)$. In Fig. 18 and we plot partial transmissions projected on the injection and outgoing paths for various asymmetric analyte bindings $\Delta_{\ell r} = 0, 0.8, 2 \times 10^{-3} \times (2\pi c)/a$.

For the situation with no analyte binding $\Delta_{\ell r} = 0$ [see Figs. 18(a) and 18(b)], transmission through the weak-coupling surface mode (central peak) consists of only one path: injection from the left surface mode and exit from the right surface mode. The linewidth of the central peak thus reflects the linewidth of the left/right surface mode. In contrast, transmission through the strong-coupling surface mode consists of multiple paths: photon can be injected from the left surface mode or the waveguide mode, and leave the photonic crystal chip via the right surface mode or the waveguide mode.

When $\Delta_{\ell r} = 0.8 \times 10^{-3}(2\pi a/c)$, the transmission through the central peak (the weak-coupling surface mode) is suppressed. Figures 18(c) and 18(d) indicate that such suppression is caused by destructive interference between two paths: injection from the waveguide mode and injection from the left surface mode. As indicated in Figs. 18(e) and 18(f), the destructive interference still exists when $\Delta_{\ell r}$ is increased to $2 \times 10^{-3}(2\pi a/c)$. However, in this case photon is mainly injected via the waveguide mode, rather than the other path. These figures also indicate other path changes in transmission at other frequencies when analyte binding modifies $\Delta_{\ell r}$.

Acknowledgments

We thank S. Foster, Q. Du, and W.-T. Lau for helpful discussions. This work was supported by the Natural Sciences and Engineering Research Council of Canada. S.F acknowledges support from the National Natural Science Foundation of China through Grant No. 11374378. J.H.J acknowledges support from start-up funding of Soochow University.

#257100 Received 13 Jan 2016; revised 17 Feb 2016; accepted 15 May 2016; published 26 May 2016